https://doi.org/10.5194/egusphere-2025-1810
Preprint. Discussion started: 16 May 2025

Technical note: Investigation into the mechanism of chemical abrasion using SHRIMP, Raman spectroscopy and atom probe tomography

Charles W. Magee, Jr[1], Lutz Nasdala[2], Renelle Dubosq[3,4], Baptiste Gault[3,5], Simon Bodorkos[1]

[1]Geoscience Australia, Canberra ACT, 2609, Australia
[2]Institut für Mineralogie und Kristallographie, Universität Wien, Josef-Holaubek-Platz 2, A-1090 Vienna, Austria
[3]Max-Planck-Institut für Nachhaltige Materialien GmbH, Düsseldorf, Germany
[4]Department of Earth, Environmental, and Geographic Sciences, The University of British Colombia Okanagan, Kelowna, BC, Canada
[5]Department of Materials, Royal School of Mines, Imperial College, London, UK

Correspondence to: Charles Magee (Charles.magee@ga.gov.au)

Abstract.

Chemical abrasion, a two-step process of annealing and partial dissolution, is routinely applied to zircon grains prior to U-Pb geochronology, to remove portions of the grains affected by Pb loss. The exact effect of this technique on the zircon structure and the distribution of radiogenic isotopes, however, remains elusive. Herein, grains of reference zircon OG1 were either fully or partially subjected to the chemical abrasion process and subsequently analysed by sensitive high mass resolution ion microprobe (SHRIMP) to determine the U-Pb systematics. Sputter craters from untreated, annealed, and fully chemically abraded aliquots were then mapped using Raman spectroscopy to determine the magnitude and distribution of radiation damage. For the untreated and annealed zircon, sputter craters from both concordant and discordant analyses were mapped. All chemically abraded zircon SHRIMP analyses were concordant. Raman mapping showed that the bottoms of discordant SHRIMP sputter craters generally had areas of higher and more heterogeneous Raman band width than concordant sputter pits for the same treatment. These results are consistent with previous scanning electron microscopy and micro computer tomography results. Based on the Raman maps, sputter craters with varying degrees of lattice damage and Pb loss were targeted for nanoscale analysis using atom probe tomography (APT) to assess the distribution of radiogenic isotopes at the lattice scale. APT reconstructions reveal a homogeneous distribution of all major components and radiogenic isotopes for all samples. These results indicate that APT is not able to detect elemental mobility or void formation arising from the lead loss, annealing or chemical abrasion in these samples. Thus the APT data do not provide additional constraints beyond the SHRIMP and Raman data on the mechanisms of Pb loss. Importantly, as the APT technique cannot distinguish between concordant and 5-10% discordant zircon, it should not be used for this purpose.

1 Introduction

1.1 Chemical abrasion

Like all isotope geochronology, uranium – lead dating becomes less repeatable and precise if either the parent or daughter products are mobilized. In zircon, lead, which is more incompatible than uranium in the zircon crystal lattice, is generally the

https://doi.org/10.5194/egusphere-2025-1810
Preprint. Discussion started: 16 May 2025

element which is mobilized. As the two naturally-occurring uranium isotopes have different decay constants, the loss of Pb will disturb the apparent ages by different amounts. This discordance in U-Pb ages offers a way to determine if Pb loss has occured in zircon, even within the vanishingly small analytical volumes of microanalytical techniques.

The accuracy and precision of zircon U-Pb dating has been substantially improved by the removal of zircon material which has undergone Pb loss via a treatment process called chemical abrasion (Mattinson 2005). The application of this technique to individual zircon crystals using a single annealing step has been widely adopted for high precision U-Pb zircon geochronology, despite imperfect knowledge of the exact details of the mechanism by which it operates (Mundil et al. 2004). While there is some variation in the modern chemical abrasion (CA) process, the current practice involves a single annealing step of 900-1000°C for a week to 16 hours, which is followed by a partial dissolution step of 8 to 16 hours in HF at 180-210°C in a pressure vessel. Zircon material which survives this partial dissolution process is described at chemically abraded.

Mattinson (2011) shows that the annealing step of the CA process alters zircon domains which have undergone Pb mobilization in such a way that they dissolve in HF at a lower temperature (~180-210°C) than isotopically closed zircon. McKanna et al. (2023, 2024) show that this dissolution happens at scales from tens of micrometres to submicrometres, and often follows zoning domains, cracks, inclusions, and other areas of mineral imperfection. However, the exact mechanism of how and why this annealed zircon becomes more susceptible to dissolution is not fully understood.

1.2 Radiation damage accumulation and annealing

Metamictization, the *in situ* destruction of a mineral's crystal structure and its eventual transformation into an amorphous phase, has been known since before the discovery of radioactivity (Brøgger 1893). Self-irradiation damage was realized soon thereafter to be the main cause of metamictization (Hamberg 1914), especially in U-bearing minerals such as zircon (Ewing 1994).

Heat-treatment of partially radiation-damaged zircon, which consists of an amorphous volume fraction and a crystalline volume fraction of variable degrees of damage, results in gradual reconstitution of the crystal structure, depending on heating temperature and duration. Recovery of partially radiation-damaged zircon in the laboratory starts at temperatures of as low as 400-500°C and progresses to about 1400°C (Zhang et al. 2000; Ende et al. 2021). The two main recovery processes are growth of crystalline remnants at the expense of the amorphous volume fraction, and recovery of lattice defects in the crystalline volume fraction, with random nucleation in the amorphous phase having insignificant contribution (Ende et al. 2021). In contrast, recovery of metamict zircon (i.e. completely amorphous $ZrSiO_4$ lacking crystalline remnants) depends on random nucleation in the glass, which does not start below about 800°C (Nasdala et al. 2002). Annealing at temperatures of about 900-1000°C results in the decomposition into oxides, namely, an amorphous silica phase and various allotropes of crystalline ZrO_2 (Ellsworth et al. 1994; Capitani et al. 2000). Metamict $ZrSiO_4$ is transformed into crystalline zircon only at high temperatures exceeding 1150°C (McLaren et al. 1994; Nasdala et al. 2002). The temperature-time range of 900-1000°C for hours to tens of hours, where decomposition into oxides occurs, corresponds to the range of annealing temperatures used for CA. Thus, as a first approximation, it is reasonable to hypothesize that the fraction of material that is preferentially dissolved

https://doi.org/10.5194/egusphere-2025-1810
Preprint. Discussion started: 16 May 2025

during the chemical abrasion process consists of metamict, or at least strongly radiation-damaged domains that have (fully or partially) recrystallized into non-zircon phases during the annealing stage, as such phases are more susceptible to dissolution than zircon.

It should be noted that annealing metamict $ZrSiO_4$ at 900-1000°C that is *not* followed by the dissolution step of CA may result in strongly reverse U-Pb discordance of SHRIMP analysis results (McLaren et al. 1994; Nasdala et al. 2002). This may be a result of differential sputtering rates of the separated phases. Additionally, results of secondary ion mass spectrometry (SIMS) analyses of baddeleyite (the most common ZrO_2 polymorph), show that the relative ionization efficiencies of Pb and U are highly variable and crystal orientation dependent (Wingate and Compston 2000).

Experiments which vary the annealing (900-1000°C) or partial dissolution conditions (180-210°C) (Huyskens et al. 2016; McKanna et al. 2023; McKanna et al. 2024) show a gradual process, where lower time and temperature treatments remove less open system material than more aggressive treatments, up to the point (1000°C) where areas with Pb loss anneal and lock in the Pb loss (Huyskens et al. 2016). Similarly, Raman band broadening due to radiation damage increases nearly linearly with damage, as opposed to having a step function. Therefore, it remains unclear exactly how lattice damage and Pb mobilization are related. It is also unclear if the minor degree of Pb loss commonly observed in a wide variety of pre-Mesozoic zircon results from scattered small areas of significant Pb loss, or large-scale pervasive Pb loss (Magee et al. 2023; Kooymans et al. 2024; Donaghy 2024). Nor is the exact relationship between the accumulation of radiation damage, Pb loss, and secondary alteration fully understood. Even metamict (fully amorphous) $ZrSiO_4$ may be concordant if no disturbing geological event was experienced (Nasdala et al. 2002). Documenting such small scale processes requires investigation using high-spatial structural and geochemical techniques such as APT.

1.3 APT studies of zircon

An atom probe is a mass spectrometer with sub-nanometre spatial resolution, in principle with a similar sensitivity to all elements in the range of 10s of ppm (Gault et al. 2010, 2021). Atom Probe Tomography (APT) is the tomographic reconstruction of the analyzed volume based on the temporal and spatial arrival of ions at the detector. This combination of high spatial and chemical resolutions makes it attractive to study property-modifying nanoscale microstructural features. Although the use of APT in Earth sciences is relatively recent, there is an array of reports of using APT on zircon, particularly zircon old enough to have accumulated enough ^{207}Pb to be detectable by APT. Valley et al. (2014) show that Hadean detrital zircons in the Mesoarchean Jack Hills Group show clusters of Pb, Y, and Al, which presumably formed in a pre-sedimentary (and thus hard to characterize) metamorphic event around 3.4 Ga. Peterman et al. (2016) show similar clusters in 2.1 Ga sedimentary zircon that were metamorphosed to granulite facies during the Mesozoic. Peterman et al. (2021) then show that these clusters can be synthesized in Archean zircons by annealing them at 1450°C. Piazolo et al. (2016) show that plastically deformed zircons from an ultra-high temperature (UHT) domain have a wider variety of trace element heterogeneities, many of which are associated with dislocation features. In contrast, Exertier et al. (2018), and Saxey et al. (2018) show that results of APT analyses of reference zircons are indeed homogenous, as were the untreated control Archean zircons of Peterman et

https://doi.org/10.5194/egusphere-2025-1810
Preprint. Discussion started: 16 May 2025

al. (2021). This difference has been used in further studies, (e.g. Greer et al. 2023), to suggest that a homogenous atom probe result implies a lack of Pb mobilization and isotopic closure in the U-Pb system.

Thus, to deepen our understanding of the Pb loss process in zircon, as well as how it is ameliorated by chemical abrasion, we investigated OG1 reference zircon grains under three conditions: untreated, annealed, and fully chemically abraded. For the untreated and annealed grains, individual SHRIMP craters that yielded concordant and discordant analyses were mapped using Raman spectroscopy to identify areas of maximum lattice damage. Those areas were then analysed using APT to investigate the distribution of the constituent atoms in these zircons in an attempt to identify potential mechanisms of Pb loss. Sputter craters from fully chemically abraded grains, all of which yielded concordant analyses, were also mapped with Raman spectroscopy and further analysed with APT.

2. Materials and methods

2.1 OG1 target zircon

The OG1 zircon (Stern et al. 2009) was selected for this study due to its well-characterized nature and extensive use as a reference zircon (Stern et al. 2009; Magee et al. 2017; Kemp et al. 2017; Petersson et al. 2019). Sourced from the Owens Gully Diorite in the Pilbara Craton, Australia, its Paleoarchean age provides a high $^{207}Pb/^{206}Pb$ ratio, making it well-suited for APT analyses, which can struggle with ^{207}Pb detection in younger zircons. Measurements of untreated zircons by both TIMS and SHRIMP identify slight Pb loss, which is ameliorated by chemical abrasion (Stern et al. 2009; Kooymans et al. 2024). Geoscience Australia has considerable amounts of OG1 material in its archives, including fully chemically abraded OG1 (in mount GA5015), and annealed but not partially dissolved material (in mount GA5005). Following crystallization at 3465 Ma, the Owens Gully Diorite underwent regional amphibolite grade metamorphism around 3.3 Ga (François et al. 2014), and the U-Th-He age of the zircons is about 750 Ma (Magee et al. 2017), indicating that it has been cool enough to accumulate radiation damage since that time.

2.2 Specimen treatment and selection

OG1 zircon grains were annealed in a quartz boat for 48 hours at 1000°C (Bodorkos et al. 2009). The chemically abraded grains were subsequently partially dissolved in HF at 200°C for 10 hours at the Royal Ontario Museum, and the annealed grains had no further treatment. Aliquots of several hundred grains were then mounted in two 25 mm epoxy disks and polished. Mount GA5005 contains untreated and annealed OG1, while mount GA5015 contains untreated and chemically abraded OG1. Both mounts contain the TEMORA-2 reference zircon (Black et al. 2004). Transmitted light, reflected light, and cathodoluminescence images of all zircons were taken prior to SHRIMP analysis. After the experiments described by Bodorkos et al. (2009), these two mounts were stored in the Geoscience Australia archive before being retrieved for this study.

https://doi.org/10.5194/egusphere-2025-1810
Preprint. Discussion started: 16 May 2025

2.3 SHRIMP U-Pb analysis

Mounts GA5005 and GA5015 were run side-by-side in a single combined SHRIMP U-Pb session on the Geoscience Australia SHRIMP IIe instrument. A primary beam of O_2^- with approximately 10.68 kV impact energy and a primary beam monitor (PBM; net sample current) current of approximately -2 nA was projected through a 100 µm aperture to sputter a flat-bottomed ellipsoidal crater approximately 16 × 21 µm^2 across and one µm deep. Secondary ions were extracted from the sample surface at approximately 675 V before being accelerated into the Matsuda mass spectrometer at 10 kV. The analyser magnet cycled six times through the standard Geoscience Australia 10 peak run table of $^{196}Zr_2O$, ^{204}Pb, background, ^{206}Pb, ^{207}Pb, ^{208}Pb, ^{238}U, ^{248}ThO, ^{254}UO, and $^{270}UO_2$. Ions were counted using a single ETP electron multiplier. Each of the six samples (untreated TEMORA-2 and OG1 on both mounts, annealed OG1, and CA OG1), was analysed 40 times. The resulting data were processed using the SHRIMP 2.5 software three times. Once using the GA5015 TEMORA-2 as the primary reference material, once using the GA5005 TEMORA-2 as the reference material, and once combining the TEMORA-2 samples from both mounts as a single reference. In all cases, the Pb/U versus UO/U calibration was used, and common Pb correction was done using the ^{204}Pb isotope and the model lead isotopic composition of Stacy and Kramers (1975).

2.4 Raman spectroscopy

The degree of accumulated radiation damage in zircon was estimated from the full width at half band maximum (FWHM) of the ca. 1000 cm^{-1} Raman band (Nasdala et al. 1995), which is assigned to antisymmetric stretching vibrations of SiO_4 tetrahedrons (Dawson et al. 1971). Analyses were done by means of a dispersive Horiba LabRAM HR Evolution spectrometer equipped with Olympus BX-series optical microscope, a diffraction grating with 1800 grooves per mm, and Peltier-cooled charge-coupled device (CCD) detector. Spectra were excited with the 632.8 nm emission of a He-Ne laser (10 mW at the sample surface), using an Olympus 100× objective (numerical aperture 0.90). Wavenumber calibration was done using the Rayleigh line. The system was operated in full confocal mode, resulting in a lateral resolution of better than 1 µm (compare Kim et al. 2020) and a depth resolution of ca. 2 µm. Hyperspectral maps were obtained using a software-controlled x-y stage in "oversampling" mode (step size in the range 0.6-0.9 µm). Fitted FWHM values were corrected for the artefact of experimental band broadening according to the procedure of Váczi (2014), based on the spectrometer's FWHM of the instrumental profile function (IPF) of 0.8 cm^{-1} in the red range. For further details see Zeug et al. (2018).

2.5 Atom probe tomography

A suite of six zircon samples were selected for APT analysis, i.e., 05U-16.1 (untreated concordant), 05U-21.1 (untreated discordant), 15U-14.1 (untreated discordant), A-23.2 (annealed concordant), A-17.1 (annealed discordant), and C-13.1 (chemically abraded concordant). A series of specimens (n=4-5) was prepared from each sample by in situ liftout (Thompson et al. 2007). The surface was protected by ion-beam deposition of a ~0.5 µm Pt layer and specimens were shaped into needles with annular milling at 30 kV on a dual-beam scanning electron microscope/focused ion beam (FEI Helios Nanolab 600i or

https://doi.org/10.5194/egusphere-2025-1810
Preprint. Discussion started: 16 May 2025

Helios Plasma-FIB) and subsequently cleaned using the ion-beam at 5 kV to remove regions potentially severely damaged by the implantation of energetic Ga or Xe ions. The specimens were then analyzed by APT in a CAMECA local electrode atom probe (LEAP) 5000 XR fitted with a reflectron lens with a detection efficiency of ~52% at the Max-Planck-Institut für Nachhaltige Materialien, Dusseldorf, Germany (Table S1). The specimens were analyzed at a base temperature of 50-60 K, with a laser pulse energy of 400-700 pJ focused on an area estimated to be <3 μm in diameter, a detection rate of 0.03-0.1 ion detected for 100 pulses and a laser pulse repetition rate of 100-200 kHz. The data processing and reconstruction were done with the commercial software packages AP Suite 6.1 and 6.3. The ranged mass spectrum used for the specimens is shown in Figure S1. A schematic showing the relative analytical volumes of SHRIMP, Raman, and APT is shown in Figure 1.

3 Results

3.1 SHRIMP U-Pb results

As both SHRIMP mounts GA5005 and GA5015 were run side-by-side it was possible to reduce the data as a single session. Treating the TEMORA-2 samples on both mounts as a single population gave the best agreement between the ages of untreated OG1 on both mounts, and these results are shown in Table 1 and Figure 2. As with Kooymans et al. (2024), the chemically abraded $^{206}Pb/^{238}U$ age is within the 95% confidence interval of the $^{207}Pb/^{206}Pb$ reference age of 3465 Ma and the chemically abraded $^{206}Pb/^{238}U$ age of 3463 Ma (Stern et al. 2009). The untreated and annealed grains yielded analyses that revealed variable Pb loss and could not be grouped in a single population. Excluding grains to form a coherent group gave weighted mean values for both the untreated OG1 zircon grains on each mount (Table 1) which are within uncertainty of the 3440 Ma $^{206}Pb/^{238}U$ TIMS age of Stern et al. (2009), and the SHRIMP ages of previous studies (Magee et al. 2023; Kooymans et al. 2024). Eleven individual SIMS sputter craters (two untreated concordant, two untreated discordant, two annealed concordant, three annealed discordant, and two CA concordant) were chosen for further study using hyperspectral Raman imaging. The U-Pb systematics of these spots are shown in Table 2.

3.2 Hyperspectral Raman mapping

The FWHM of the main zircon Raman band near 1000 cm^{-1} is 1.7-1.8 cm^{-1} for well-ordered zircon (Nasdala et al. 2002; Zeug et al. 2018) and increases to well above 30 cm^{-1} at elevated stages of damage accumulation (Nasdala et al. 1995; Zhang et al. 2000). In the present study, FWHM values between 3.2 and 32 cm^{-1} were obtained (Table 3), characterizing the samples as spanning almost the entire range from mildly to severely radiation-damaged. Untreated grains of OG1 are in general moderately to severely radiation-damaged (FWHMs in the range 10-32 cm^{-1}), with significant zoning and/or patchy heterogeneity on a scale of within single SHRIMP spots. This is new information, as the OG1 reference zircon has, to the best of our knowledge, never been subjected to any systematic quantitative study of the structural state and its internal heterogeneity, even though cathodoluminescence (CL) images obtained from polished grains indicated some degree of internal

https://doi.org/10.5194/egusphere-2025-1810
Preprint. Discussion started: 16 May 2025

structural zonation (Stern et al. 2009; for the dependence of luminescence intensity on radiation damage see Nasdala et al. 2002; Lenz and Nasdala 2015).

Band widths for the annealed and chemically abraded grains (FWHMs 3-12 cm^{-1}) were in general much narrower than that of the untreated grains. Based on results of recent annealing studies (Ginster et al. 2019; Ende et al. 2021), the above FWHM values (obtained after samples had experienced 48 h at 1000°C) indicate initial FWHMs of 6-30 cm^{-1} before annealing. There are no systematic differences between structural states of annealed-only and annealed plus chemically abraded samples. Neither are there systematic differences in degrees of radiation damage between concordant and discordant spots, even though the latter seem to be slightly more heterogeneous. Most of the discordant grains yielded heterogeneous FWHM distribution patterns across the SHRIMP analysis pits (Figure 3). There are generally zones or linear features in the sputter crater maps, showing areas of narrower and wider bands.

3.3 APT results

A total of 22 specimens from the six zircon samples were successfully analyzed with APT. All datasets yield similar compositions for zircon major components (i.e., 17.4-21.1 at% Zr; 14.6-17.1 at% Si; and 57.3-62.3 at% O; Table 4). Other element species detected in APT include H, Hf, Y, Pb, Li, Yb, U, Th, Lu, and Tm (Table 4). To evaluate the measurement reliability, the composition of zircon components (Zr, Si, O, H, Y, Pb, Li, Hf, and U) is plotted against the estimated electric field for each dataset (Figure S2). The electric field strength during experiments is approximated using the charge-state ratio of Si^{2+}/Si^{+} as a proxy. The plots indicating the composition versus field estimate for each of the mentioned species show no apparent trends across datasets from the same sample, thus validating the comparison of the composition obtained from the different experiments. Furthermore, there are no significant trends in compositions between treatment types or Pb retention, indicating similar compositions across samples. The only discernible trend is observed for Y, Pb, and Li, where their compositions are slightly higher in annealed samples compared to chemically abraded and untreated samples. Similarly, the compositions of the same species across different regions of interest within a single specimen (sample 05A-23.2, dataset 78075) was plotted against the estimated field for each region to assess the stability of APT experiments during extended runs (>6hrs; Figure S3). Throughout a single analysis, the electric field displays minimal variation, with Si^{2+}/Si^{+} ratios ranging from 17.35 to 17.81, while compositions remain consistent despite the minimally fluctuating field.

All datasets had minor 103 Da and 103.5 Da peaks (^{206}Pb and ^{207}Pb, respectively) above background, however, the major Pb peak at 104 Da (^{208}Pb) overlaps with $^{28}Si_2{}^{16}O_3{}^{+}$ (Figure 4, S1, S4). Therefore, only the peaks at 103 and 103.5 Da are considered in the bulk composition analysis and used to evaluate the distribution of Pb in the datasets. The 3D reconstructions of all datasets reveal a homogeneous distribution of Pb and every other major or trace element (Figure S5) with the exception of Li in sample 05A-23.2 (annealed concordant; Figure 5a). A nearest neighbor analysis, which measures the distance between each Pb ion and its closest Pb ion neighbor (d-pair) and plots it against a randomized distribution of ions, confirms the homogeneity of Pb distribution in each sample (Figure 6a-f). The homogeneous distribution of Pb is also confirmed in each

https://doi.org/10.5194/egusphere-2025-1810
Preprint. Discussion started: 16 May 2025

sample by performing a radial distribution analysis whereby the bulk normalized composition of each species is plotted as a function of its radial distance to the nearest Pb ion (Figure 6g-l). Since the bulk composition of Pb hovers about a value of 1 for each dataset, homogeneity can be assumed. In sample 05A-23.2 (annealed concordant), the frequency distribution of the d-pair distances for Li is skewed towards lower distances when compared to the randomized distribution curve, suggesting inhomogeneity (Figure 5b). The radial distribution analysis of Li for sample 05A-23.2 reveals elevated bulk normalized compositions of Li for short radial distances, also confirming the heterogeneous distribution of Li in the sample (Figure 5b, 5c).

4. Discussion

4.1 SHRIMP U-Pb

The SHRIMP U-Pb results are consistent with previous work on this topic. Kooymans et al. (2024) show a similar difference in U-Pb dates between chemically abraded and untreated OG1 zircon. Our results are consistent with the ~10,000 archived SHRIMP analyses reported in Kooymans et al. (2024) showing a median $^{206}Pb/^{238}U$ date of ~3440 Ma for untreated OG1, similar to the results reported in Magee et al. (2023) and Stern et al. (2009). The grouped mean of the annealed OG1 $^{206}Pb/^{238}U$ date was intermediate between the untreated and chemically abraded grains, but it is interesting that the discordant spots in annealed OG1 are more discordant than in the untreated samples (Figure 2).

4.2 Raman

Untreated discordant zircon tended to have regions where the FWHM exceeded 30 cm^{-1}, while in concordant zircon the maximum FWHM was generally less than 25 cm^{-1} (Table 3). This reconfirms that radiation damage lowers the Pb retention performance of zircon. As expected, after annealing (without and with additional CA), zircon is much less radiation-damaged than before treatment, indicated by significantly narrower Raman FWHMs. Here, degrees of damage of discordant and concordant spots overlap, making clear conclusions impossible. Concordant and discordant spots (in both untreated and annealed/CA grains) differ insofar as discordant samples show somewhat higher extents of structural heterogeneity across the SHRIMP analysis pit (Figure 3). Overall, Raman spectroscopy alone does not give conclusive hints to why annealed zircon yields concordant or discordant Pb/U ratios. Raman response of chemically abraded samples were similar to the annealed ones in terms of peak width. CA pits had few features visible in Raman.

4.3 Nanoscale element distribution

Elements detected include O, Si, Zr, H, Hf, Y, Pb, Li, Yb, Lu, Tm, U, and Th. Hydrogen is considered to be a contaminant from the vacuum. Nearly all zircon components revealed a homogenous distribution in all specimens, with the single exception of Li in 05A-23.2. Aluminium was not detected. This is not surprising given the near-mantle O isotope values of OG1 (Avila et al. 2020), which indicate minimal crustal assimilation by the parental magma, and the low (< 3 ppm) Al concentrations

https://doi.org/10.5194/egusphere-2025-1810
Preprint. Discussion started: 16 May 2025

recorded in previous studies of OG1 zircon (Kooymans et al. 2024). In contrast, yttrium is abundant in OG1 zircons, with Kooymans et al. (2024) reporting median values in excess of 1000 ppm. None-the-less, there is no evidence of clumping of Y and / or Pb in any of the analysed APT specimens. This suggests that the regional amphibolite grade metamorphism (François et al. 2014) which gives the Owens Gully Diorite its foliation was not hot or long enough to initiate the Pb ± Y ± Al clump formation seen in zircons subject to hotter granulite or UHT conditions (Peterman et al. 2016; Piazolo et al. 2016). Phosphorus was not detected; therefore spatial correlation between Y and P was not possible.

Since all elemental distributions are homogenous across all specimens, no discernible differences can be attributed to the treatment types at the tens to hundreds of nm scale of APT. Similarly, no differences are observed between discordant and concordant grains. This particularly significant because it indicates that APT is not effective as a sole technique to assess isotopic disturbances such as Pb loss. SHRIMP analyses with up to 9% discordance yield APT results that are homogenous and identical to concordant grains, despite being from areas with the highest levels of lattice damage, as shown by Raman spectroscopy. Potential explanations for the homogeneous distribution of elements are discussed below. Based on these data, we suggest that APT not be used as the sole method for determining closure in the U-Pb system for zircon.

McKanna et al. (2023) show that CA produces voids down to the sub-micron limit of their spatial resolution. Wang et al. (2020) demonstrate that APT can detect voids in metal alloys in the form of artefacts showing apparent clustering or dispersion of matrix ions due to trajectory aberrations during evaporation caused by the distortion of the electrostatic field created by the void. Dubosq et al. (2020) demonstrate that this technique can also be used in geologic materials by identifying voids in the form of fluid inclusions in Archean pyrite. As all elements in the atom probe results from the chemically abraded sample (C-13.1) are homogenous, we have no evidence that CA produces voids at the nanometre scale of Dubosq et al. (2020)'s fluid inclusions.

The homogenous distribution of Si and Zr in the annealed samples (A-17.1, A-23.2) suggests that the formation of amorphous silica and ZrO_2 through annealing metamict zircon at similar temperatures, as demonstrated by McLaren et al. (1994) has not occurred in any of the eight ATP tips successfully run from these samples.

4.4 Potential Mechanisms of Pb loss

4.4.1 Homogenous Pb loss

We know from the U-Pb data that the discordant spots in this study have lost Pb. Whether this Pb loss was homogenous or heterogeneous on the scale of the SHRIMP sputter crater depends on how we interpret this data. The collected data are consistent with small degrees of uniform Pb loss from substantial portions of the zircon volume. This, in turn, is consistent with the consistently lower U-Pb ages of natural OG1 compared to chemically abraded grains (Kooymans et al. 2024). Peterson et al. (2016) suggest that Pb loss can be enhanced in zircon with radiation damage above the first percolation point, which was suggested to be reached after sustaining 3.5×10^{18} alpha decays per g (Salje et al. 1999). However, Salje et al. (1999) had obtained their results from zircon from Sri Lanka. This material is known to have experienced significant damage annealing

https://doi.org/10.5194/egusphere-2025-1810
Preprint. Discussion started: 16 May 2025

(Palenik et al. 2003; Nasdala et al. 2004), resulting in accumulation of only about 55% of all radiation damage experienced. In view of these findings, the first percolation point of Salje et al. rather corresponds to an effective self-irradiation (without any annealing) of 2×10^{18} α/g. The first percolation point is associated with Raman FWHMs of about 25 cm^{-1} (Palenik et al. 2003; Nasdala et al. 2004). Such broadened Raman bands have been obtained from discordant (untreated) zircon (Table 3). Our results are hence consistent with radiation-damage-enhanced volume diffusion of Pb out of the zircon.

However, a homogenous Pb loss model is not consistent with the work of McKanna et al. (2023; 2024), who showed that chemical abrasion attacks discrete domains in zircon in a highly heterogeneous manner. As the Raman maps for the discordant SHRIMP spots are also heterogeneous in radiation damage (as observed by local variations of Raman band widths), heterogeneous models of Pb loss should be considered, especially if they can be reconciled with the APT results.

4.4.2 Heterogeneous Pb loss

Micrometre-to submicron-scale heterogeneity needs to be considered as one feature potentially favouring secondary loss of radiogenic Pb. Heterogeneous volume expansion of neighbouring sample volumes results in complex strain patterns and, if the elasticity maximum is exceeded, the opening of fractures that then may serve as ideal pathways for fluids (Peterman et al. 1986; Chakoumakos et al. 1987; Lee and Tromp 1995; Nasdala et al. 2010). However, on the resolution scale of a powerful optical microscope, such fractures were not always observed (which however does not rule out their existence). Nonetheless, McKanna et al. (2023; 2024) show that chemical abrasion selectively dissolves zircon in such a manner down to the limit of their imaging resolution (about half a micron) and that the leachate solutions from the CA partial dissolution have disturbed U-Pb systematics.

If the discordant areas in zircon are discrete areas of damage distributed within a matrix of isotopically closed zircon, there is a possibility that sampling might miss these regions purely by chance. The likelihood of missing the damaged areas by chance depends on distribution of Pb loss. If disturbed regions are a mix of intact and damaged areas, the probability of randomly sampling only the intact areas is low, calculated as (1-damaged fraction) ^ n. Considering a SHRIMP spot with 5% Pb loss, where the Raman can exclude 75% of the spot area as having lost Pb, the remaining 25% of the spot would then account for the Pb loss. Given this scenario, the remaining area would have experienced a 20% Pb loss. The most extreme possibility is that 20% of this area has lost 100% of its Pb, and the remaining 80% is concordant. As this study had nine successful APT analyses (on three discordant grains), the probability of choosing concordant areas by chance is 0.8^9, or 13%. It is important to note that this is a maximum, assuming total Pb loss from the altered areas. McKanna et al. (2024) show that the areas altered enough for chemical abrasion to dissolve them still contain significant Pb. If instead we assume that 40% of the area has suffered 50% Pb loss, then the probability of sampling only the intact areas drops to 1% (0.6^9).

Of course, these estimates assume that APT analytical volumes can be chosen and run without bias. It is interesting that of the eight specimens which failed while being run in the Atom Probe, six were from discordant SHRIMP spots. As the accumulation of radiation damage involves substantial volume increase, heterogeneous self-irradiation of zoned zircon will necessarily result in complex strain patterns (compressive in more, and dilative in less damaged volumes). Fracture of APT

https://doi.org/10.5194/egusphere-2025-1810
Preprint. Discussion started: 16 May 2025

specimens is generally assumed to be caused by the electrostatic pressure arising from the intense electrostatic field used to field evaporate the surface atoms over the course of the experiment, making brittle materials more prone to early fracture (Wilkes et al. 1972). If strained polyphase material leads to an enhanced propensity for specimen failure before any APT data can be acquired, then there will be a strong selection bias in the results favouring intact zircon. We are not aware of any successful APT analyses of metamict zircon in the literature, either on purpose or by accident. While the inherited cores analysed by Peterman et al. (2016) show Pb loss, that material was reannealed in Mesozoic granulite facies metamorphism, and has had minimal radiation damage accumulation since then. It is possible that the APT analytical technique gives a Panglossian view of zircon crystal chemistry, by destroying badly disturbed samples instead of analysing them.

5. Conclusions

The present study shows that discordant SHRIMP spot analyses were obtained from severely radiation-damaged spots (as indicated by strongly broadened Raman bands). Annealing the zircon samples reduces the band widths in both discordant and concordant zircon, while discordant spots have more residual heterogeneity in their Raman maps. Never-the-less, APT analysis of concordant, discordant, untreated, annealed, and chemically abraded OG1 all show homogenous distribution of all detected major and minor elements, including U and Pb. As a result, APT cannot identify any differences between concordant SHRIMP spots and those which are up to 7% discordant. We therefore recommend that APT not be used as a method for determining closure in the U-Pb system for zircon. The similarity between APT results from untreated, annealed, and chemically abraded zircon is difficult to interpret, but does show that the Pb and Y cluster formation found in high temperature metamorphism and experimental tests does not appear at the temperatures and times used for chemical abrasion.

Author contributions

CM and SB designed and initiated the experiment. CM did the SIMS analysis. LN did the Raman analysis. RD and BG did the Atom Probe analysis. All authors contributed to the text, figures, and tables.

Acknowledgements

This paper is published with the permission of the CEO, Geoscience Australia.

References

Ávila, J. N., Holden, P., Ireland, T. R., Lanc, P., Schram, N., Latimore, A., Foster, J. J., Williams, I. S., Loiselle, L., and Fu, B.: High-precision oxygen isotope measurements of zircon reference materials with the SHRIMP-SI, Geostand. Geoanal. Res., 44, 85-102, https://doi.org/10.1111/ggr.12298, 2020.

https://doi.org/10.5194/egusphere-2025-1810
Preprint. Discussion started: 16 May 2025

Bodorkos, S., Stern, R. A., Kamo, S. L., Corfu, F., and Hickman, A. H.: OG1: A natural reference material for quantifying SIMS instrumental mass fractionation (IMF) of Pb isotopes during zircon dating, Eos Trans. AGU, 90, Fall Meet. Suppl., Abstract V33B-2044, 2009.

Brøgger, W.C.A.: Amorf. In: Salmonsens Store Illustrerede Konversationsleksikon 1, Brødrene Salmonsen, Kopenhagen, pp. 742-743, 1893.

Capitani, G.C., Leroux, H., Doukhan, J.C., Ríos, S., Zhang, M., and Salje, E.K.H.: A TEM investigation of natural metamict zircons: structure and recovery of amorphous domains, Phys. Chem. Miner., 27(8), 545-556, https://doi.org/10.1007/s002690000100, 2000.

Chakoumakos, B. C., Murakami, T., Lumpkin, G. R., and Ewing, R. C.: Alpha-decay-induced fracturing in zircon: The transition from the crystalline to the metamict state, Science, 236, 1556-1559, 1987.

Dawson P., Hargreave M. M., and Wilkinson G. F.: The vibrational spectrum of zircon ($ZrSiO_4$), J. Phy. C: Solid State Phys., 4, 240-256, 1971.

Donaghy, E. E., Eddy, M. P., Moreno, F., and Ibañez-Mejia, M.: Minimizing the effects of Pb loss in detrital and igneous U-Pb zircon geochronology by CA-LA-ICP-MS, Geochronology, 6, 89-106, https://doi.org/10.5194/gchron-6-89-2024, 2024.

Dubosq, R., Gault, B., Hatzoglou, C., Schweinar, K., Vurpillot, F., Rogowitz, A., Rantitsch, G., and Schneider, D.A.: Analysis of nanoscale fluid inclusions in geomaterials by atom probe tomography: Experiments and numerical simulations, Ultramicroscopy, 218, 113092, https://doi.org/10.1016/j.ultramic.2020.113092, 2020.

Ellsworth, S., Navrotsky, A., and Ewing, R.C.: Energetics of radiation damage in natural zircon ($ZrSiO_4$),Phys. Chem. Miner., 21(3), 140-149, https://doi.org/10.1007/BF00203144, 1994.

Ende, M., Chanmuang N., C., Reiners, P. W., Zamyatin, D. A., Gain, S. M., Wirth, R., and Nasdala, L.: Dry annealing of radiation-damaged zircon: Single-crystal X-ray and Raman spectroscopy study, Lithos, 406-407, 106523, https://doi.org/10.1016/j.lithos.2021.106523, 2021.

Ewing, R.C.: The metamict state: 1993—the centennial, Nucl. Instrum. Methods Phys. Res. B, 91(1-4), 22-29, https://doi.org/10.1016/0168-583X(94)96186-7, 1994.

Exertier, F., La Fontaine, A., Corcoran, C., Piazolo, S., Belousova, E., Peng, Z., Gault, B., Saxey, D.W., Fougerouse, D., Reddy, S.M., and Pedrazzini, S.: Atom probe tomography analysis of the reference zircon gj-1: An interlaboratory study, Chem. Geol., 495, 27-35, https://doi.org/10.1016/j.chemgeo.2018.07.031, 2018.

François, C., Philippot, P., Rey, D., and Rubatto, D.: Burial and exhumation during Archean sagduction in the East Pilbara Granite-Greenstone Terrane, Earth Planet. Sci. Lett., 396, 235-251, http://dx.doi.org/10.1016/j.epsl.2014.04.025, 2014.

Gault, B., Chiaramonti, A., Cojocaru-Mirédin, O., Stender, P., Dubosq, R., Freysoldt, C., Kumar Makineni, S., Li, T., Moody, M. P., and Cairney, J. M.: Atom probe tomography. Nat. Rev. Methods Primers, 1, 51, https://doi.org/10.1038/s43586-021-00047-w, 2021.

https://doi.org/10.5194/egusphere-2025-1810
Preprint. Discussion started: 16 May 2025

Gault, B., Moody, M.P., De Geuser, F., La Fontaine, A., Stephenson, L.T., Haley, D., and Ringer, S.P.: Spatial resolution in atom probe tomography, Microsc. Microanal., 16(1), 99–110, https://doi.org/10.1017/S1431927609991267, 2010.

Ginster, U., Reiners, P.W., Nasdala, L., and Chanmuang N., C.: Annealing kinetics of radiation damage in zircon, Geochim. Cosmochim. Ac., 249, 225-246, https://doi.org/10.1016/j.gca.2019.01.033, 2019.

Greer, J., Zhang, B., Isheim, D., Seidman, D.N., Bouvier, A., and Heck, P.R.: 4.46 Ga zircons anchor chronology of lunar magma ocean, Geochem. Perspect. Lett., 27, 49-53, https://doi.org/10.7185/geochemlet.2334, 2023.

Hamberg, A.: Die radioaktiven Substanzen und die geologische Forschung. Eine Übersicht, Geologiska Föreningen i Stockholm Förhandlingar, 36(1), 31-96, 1914.

Howard, B.L., Sharman, G.R., Crowley, J.L., and Wersan, E.R.: The leaky chronometer: Evidence for systematic cryptic Pb loss in laser ablation U-Pb dating of zircon relative to CA-TIMS, Terra Nova, https://doi.org/10.1111/ter.12742, 2024.

Huyskens M. H., Zink, S., and Amelin, Y.: Evaluation of temperature-time conditions for the chemical abrasion treatment of single zircons for U-Pb geochronology Chem. Geol., 438, 25-35, https://doi.org/10.1016/j.chemgeo.2016.05.013, 2016.

Kemp, A.I.S., Vervoort, J.D., Bjorkman, K., and Iaccheri, L.M.: Hafnium isotope characteristics of Palaeoarchaean zircon OG1/PGC from the Owens Gully Diorite, Pilbara Craton, Western Australia, Geostand. Geoanal. Res., 41(4), 659-673, https://doi.org/10.1111/ggr.12182, 2017.

Kim, Y., Lee, E. J., Roy, S., Sharbirin, A. S., Ranz, L.-G., Dieing, T., and Kim, J.: Measurement of lateral and axial resolution of confocal Raman microscope using dispersed carbon nanotubes and suspended graphene, Curr. Appl. Phys., 20, 71-77, https://doi.org/10.1016/j.cap.2019.10.012, 2020.

Kooymans, C., Magee, C. W. J., Waltenberg, K., Evans, N. J., Bodorkos, S., Amelin, Y., Kamo, S. L., and Ireland, T.: Effect of chemical abrasion of zircon on SIMS U-Pb, d^{18}O, trace element, and LAICPMS trace element and Lu-Hf isotopic analysis. GChron, 6, 337-363, https://doi.org/10.5194/gchron-6-337-2024, 2024.

Lee J. K. W. and Tromp, J.: Self-induced fracture generation in zircon, J. Geophys. Res.: Solid Earth, 100, 17753-17770, 1995.

Lenz, C. and Nasdala, L.: A photoluminescence study of REE^{3+} emissions in radiation-damaged zircon, Am. Mineral., 100, 1123-1133, http://dx.doi.org/10.2138/am-2015-4894CCBYNCND, 2015.

Magee, C. W. Jr., Danišík, M., and Mernagh, T.: Extreme isotopologue disequilibrium in molecular SIMS species during SHRIMP geochronology. Geosci. Instrum. MethodsData Syst., 6(2), 523-536, https://doi.org/10.5194/gi-6-523-2017, 2017.

Magee, C. W. Jr., Bodorkos, S., Lewis, C. J., Crowley, J. L., Wall, C. J., and Friedman, R. M.: Examination of the accuracy of SHRIMP U-Pb geochronology based on samples dated by both SHRIMP and CA-TIMS, GChron, 5, 1-19, https://doi.org/10.5194/gchron-5-1-2023, 2023.

Mattinson, J. M.: Zircon U-Pb chemical abrasion ("CA-TIMS") method: Combined annealing and multi-step partial dissolution analysis for improved precision and accuracy of zircon ages, Chem. Geol.., 220, 47-66, https://doi.org/10.1016/j.chemgeo.2005.03.011, 2005.

https://doi.org/10.5194/egusphere-2025-1810
Preprint. Discussion started: 16 May 2025

Mattinson, J.M.: Extending the Krogh legacy: development of the CA-TIMS method for zircon U-Pb geochronology, Can. J. Earth Sci., 48, 95-105, https://doi.org/10.1139/E10-023, 2011.

McKanna, A. J., Koran, I., Schoene, B., and Ketcham, R. A.: Chemical abrasion: the mechanics of zircon dissolution, GChron, 5, 127-151, https://doi.org/10.5194/gchron-5-127-2023, 2023.

McKanna, A. J., Schoene, B., and Szymanowski, D.: Geochronological and geochemical effects of zircon chemical abrasion: insights from single-crystal stepwise dissolution experiments, GChron, 6, 1-20, https://doi.org/10.5194/gchron-6-1-2024, 2024.

McLaren, A.C., Gerald, J.F., and Williams, I.S.: The microstructure of zircon and its influence on the age determination from Pb/U isotopic ratios measured by ion microprobe. Geochim. Cosmochim. Ac., 58(2), 993-1005, https://doi.org/10.1016/0016-7037(94)90521-5, 1994.

Mundil, R., Ludwig, K. R., Metcalfe, I., and Renne, P. R.: Age and timing of the Permian mass extinctions: U/Pb dating of closed-system zircons. Science, 305, 1760-1763, https://doi.org/10.1126/science.1101012, 2004.

Nasdala, L., Irmer, G., and Wolf, D.: The degree of metamictization in zircons: a Raman spectroscopic study, Eur. J. Mineral., 7, 471-478, 1995.

Nasdala, L., Lengauer, C.L., Hanchar, J. M., Kronz, A., Wirth, R., Blanc, P., Kennedy, A. K., and Seydoux-Guillaume, A.-M.: Annealing radiation damage and the recovery of cathodoluminescence, Chem. Geol., 191, 121-140, 2002.

Nasdala, L., Reiners, P.W., Garver, J.I., Kennedy, A.K., Stern, R.A., Balan, E., and Wirth, R.: Incomplete retention of radiation damage in zircon from Sri Lanka. Am. Mineral., 89(1), 219-231, 2004.

Nasdala, L., Hanchar, J. M., Rhede, D., Kennedy, A. K., and Váczi, T.: Retention of uranium in complexly altered zircon: An example from Bancroft, Ontario. Chem. Geol., 269, 290-300, https://doi.org/10.1016/j.chemgeo.2009.10.004, 2010.

Palenik, C.S., Nasdala, L., and Ewing, R.C.: Radiation damage in zircon. Am. Mineral., 88(5-6), 770-781, 2003.

Peterman, Z.E., Zartman, R.E., and Sims, P.K.: A protracted Archean history in the Watersmeet gneiss dome, northern Michigan. Bull. U.S. Geol. Surv., 1622, 51-64, 1986.

Peterman, E.M., Reddy, S.M., Saxey, D.W., Snoeyenbos, D.R., Rickard, W.D., Fougerouse, D., and Kylander-Clark, A.R.: Nanogeochronology of discordant zircon measured by atom probe microscopy of Pb-enriched dislocation loops, Sci. Adv., 2(9), e1601318. https://doi.org/10.1126/sciadv.160131, 2016.

Peterman, E.M., Reddy, S. M., Saxey, D. W., Fougerouse, D., Quadir, M. Z., and Jercinovic, M. J.: Trace-element segregation to dislocation loops in experimentally heated zircon. Am. Mineral., 106, 1971-1979, https://doi.org/10.2138/am-2021-7654, 2021.

Petersson, A., Kemp, A. I. S., Hickman, A. H., Whitehouse, M. J., Martin, L., and Gray, C. M.: A new 3.59 Ga magmatic suite and a chondritic source to the east Pilbara Craton, Chem. Geol., 511, 51-70, https://doi.org/10.1016/j.chemgeo.2019.01.021, 2019.

https://doi.org/10.5194/egusphere-2025-1810
Preprint. Discussion started: 16 May 2025

Piazolo, S., La Fontaine, A., Trimby, P., Harley, S., Yang, L., Armstrong, R., and Cairney, J.M.: Deformation-induced trace element redistribution in zircon revealed using atom probe tomography. Nat. Commun., 7(1), 10490, https://doi.org/10.1038/ncomms10490, 2016.

Salje, E.K.H., Chrosch, J., and Ewing, R.C.: Is "metamictization" of zircon a phase transition? Am. Mineral., 84(7-8), 1107-1116, https://doi.org/10.2138/am-1999-7-813, 1999.

Saxey, D.W., Reddy, S.M., Fougerouse, D., and Rickard, W.D.: The optimization of zircon analyses by laser-assisted atom probe microscopy: Insights from the 91500 zircon standard, In: Moser, D.E., Corfu F., Darling, J.R., (Editor), Reddy, S.M. and Tait, K. (Eds.) Microstructural Geochronology: Planetary records down to atom scale, pp. 293-313. https://doi.org/10.1002/9781119227250.ch14, 2018.

Schoene, B., Crowley, J.L., Condon, D.J., Schmitz, M.D., and Bowring, S.A.: Reassessing the uranium decay constants for geochronology using ID-TIMS U-Pb data. Geochim. Cosmochim. Ac., 70(2), 426-445, https://doi.org/10.1016/j.gca.2005.09.007, 2006.

Stacey, J.T. and Kramers, J.D.: Approximation of terrestrial lead isotope evolution by a two-stage model. Earth and planetary science letters, 26(2), pp.207-221. https://doi.org/10.1016/0012-821X(75)90088-6 1975.

Stern, R. A., Bodorkos, S., Kamo, S. L., Hickman, A. H., and Corfu, F.: Measurement of SIMS instrumental mass fractionation of Pb isotopes during zircon dating, Geostand. Geoanal. Res., 33, 145-168, https://doi.org/10.1111/j.1751-908X.2009.00023.x, 2009.

Thompson, K., Lawrence, D., Larson, D. J., Olson, J. D., Kelly, T. F., and Gorman, B.: In situ site-specific specimen preparation for atom probe tomography, Ultramicroscopy, 107, 131-139, https://doi.org/10.1016/J.ULTRAMIC.2006.06.008, 2007.

Váczi, T.: A new, simple approximation for the deconvolution of instrumental broadening in spectroscopic band profiles, Appl. Spectrosc., 68, 1274-1278, 10.1366/13-07275, 2014.

Valley, J.W., Cavosie, A.J., Ushikubo, T., Reinhard, D.A., Lawrence, D.F., Larson, D.J., Clifton, P.H., Kelly, T.F., Wilde, S.A., Moser, D.E., and Spicuzza, M.J.: Hadean age for a post-magma-ocean zircon confirmed by atom-probe tomography, Nature Geosci., 7(3), 219-223. https://doi.org/10.1038/ngeo2075, 2014.

Wang, X., Hatzoglou, C., Sneed, B., Fan, Z., Guo, W., Jin, K., Chen, D., Bei, H., Wang, Y., Weber, W.J., and Zhang, Y.: Interpreting nanovoids in atom probe tomography data for accurate local compositional measurements, Nat. Commun., 11(1), 1022, https://doi.org/10.1038/s41467-020-14832-w, 2020.

Wilkes, T. J., Titchmarsh, J. M., Smith, G. D. W., Smith, D. A., Morris, R. F., Johnson, S., Godfrey, T. J., and Birdseye, P.: The fracture of field-ion microscope specimens, J. Phys. D: Appl. Phys., 5, 2226, https://doi.org/10.1088/0022-3727/5/12/312, 1972.

Wingate, M.T.D. and Compston, W.: Crystal orientation effects during ion microprobe U-Pb analysis of baddeleyite, Chem. Geol., 168(1-2), 75-97, https://doi.org/10.1016/S0009-2541(00)00184-4, 2000.

https://doi.org/10.5194/egusphere-2025-1810
Preprint. Discussion started: 16 May 2025

Zeug, M., Nasdala, L., Wanthanachaisaeng, B., Balmer, W. A., Corfu, F., and Wildner, M.: Blue zircon from Ratanakiri, Cambodia, J. Gemmol., 36(2), 112-132, https://doi.org/10.15506/JoG.2018.36.2.112, 2018.

Zhang M., Salje E K.H., Capitani G.C., Leroux H., Clark A.M., Schlüter J., and Ewing R.C.: Annealing of α-decay damage in zircon: a Raman spectroscopic study, J. Phys.: Condens. Matter, 12(13), 3131-3148, https://doi.org/10.1088/0953-8984/12/13/321, 2000.

https://doi.org/10.5194/egusphere-2025-1810
Preprint. Discussion started: 16 May 2025

Figures and captions:

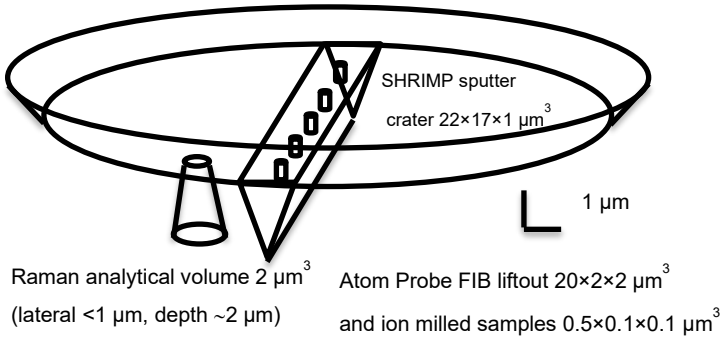

Figure 1: A scaled drawing showing the relative analytical volume of the SHRIMP, Raman, and APT analytical techniques. The SHRIMP and APT are destructive, while the Raman is not.

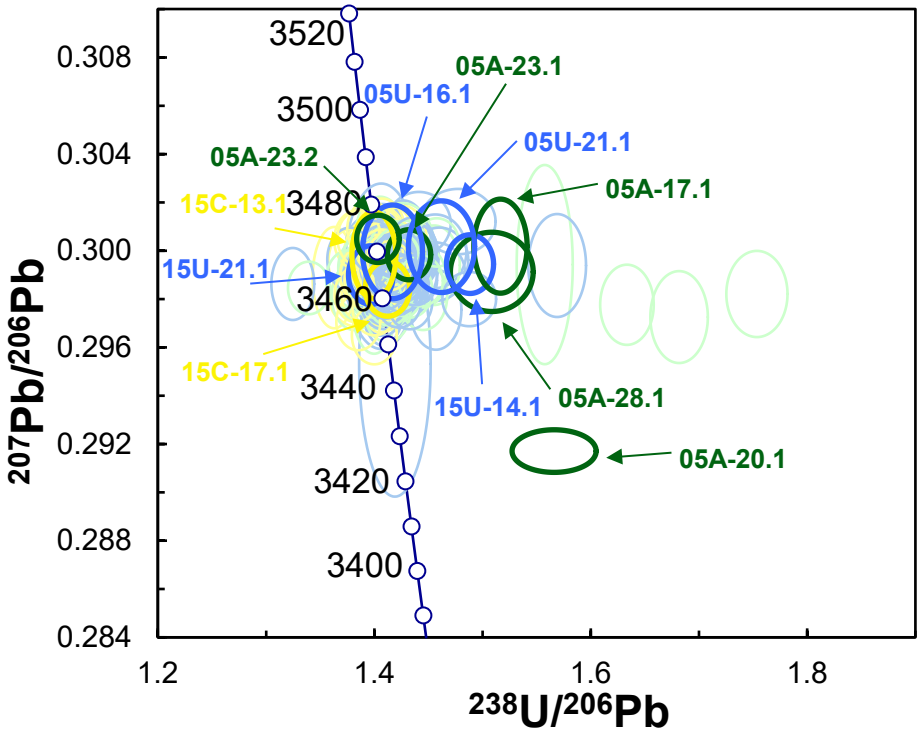

Figure 2: Concordia diagram of OG1 SHRIMP geochronology results. Untreated zircons are blue. Annealed zircons are green. Chemically abraded zircons are yellow. Analytical spots selected for APT analyses are highlighted and labelled. Data-point error ellipses represent the 68.3% confidence level.

https://doi.org/10.5194/egusphere-2025-1810
Preprint. Discussion started: 16 May 2025

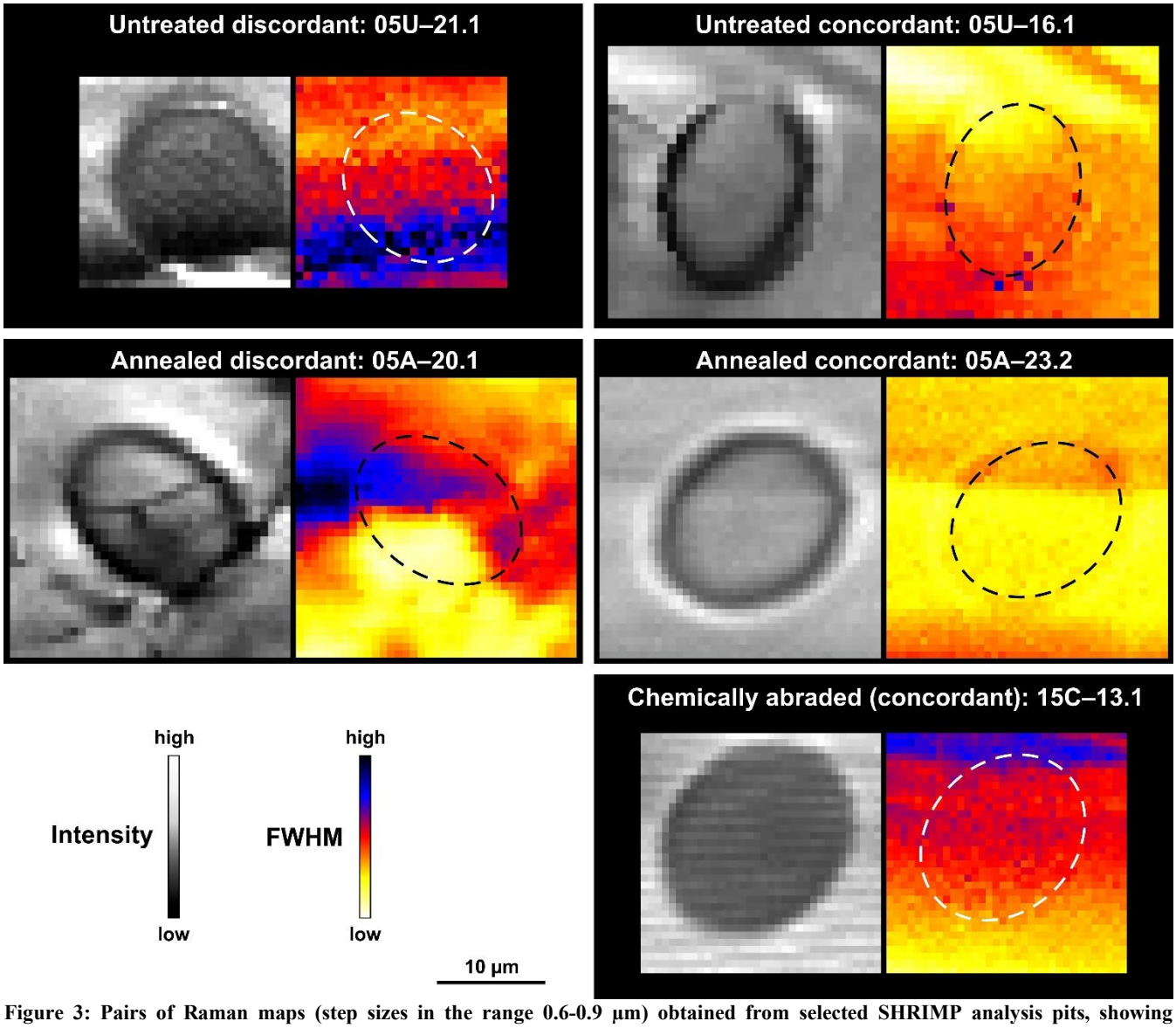

Figure 3: Pairs of Raman maps (step sizes in the range 0.6-0.9 µm) obtained from selected SHRIMP analysis pits, showing distribution patterns of fitted parameters of the main $\nu_3(SiO_4)$ zircon band near 1000 cm^{-1}. Left, intensity on an arbitrary grayscale, visualising the locations of spots. Right, FWHM (the locations of SHRIMP pits are visualised by dashed ovals). Colour-coded FWHM ranges (given in cm^{-1}) are 10-28 (05U-21.1; 05U-16.1), 4-12 (05A-20.1), 3-7 (05A-23.2) and 4-9 (15C-13.1), respectively.

https://doi.org/10.5194/egusphere-2025-1810
Preprint. Discussion started: 16 May 2025

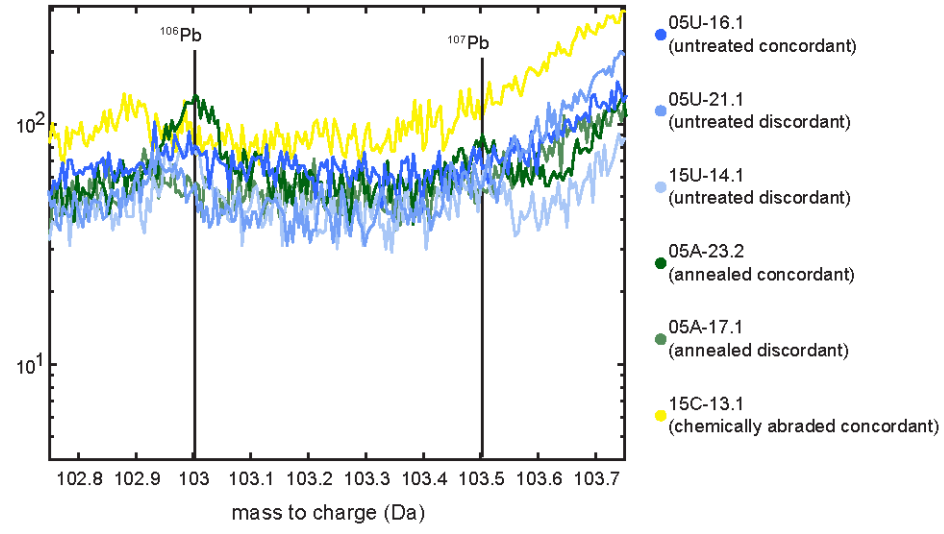

Figure 4: ^{206}Pb and ^{207}Pb spectra from each sample.

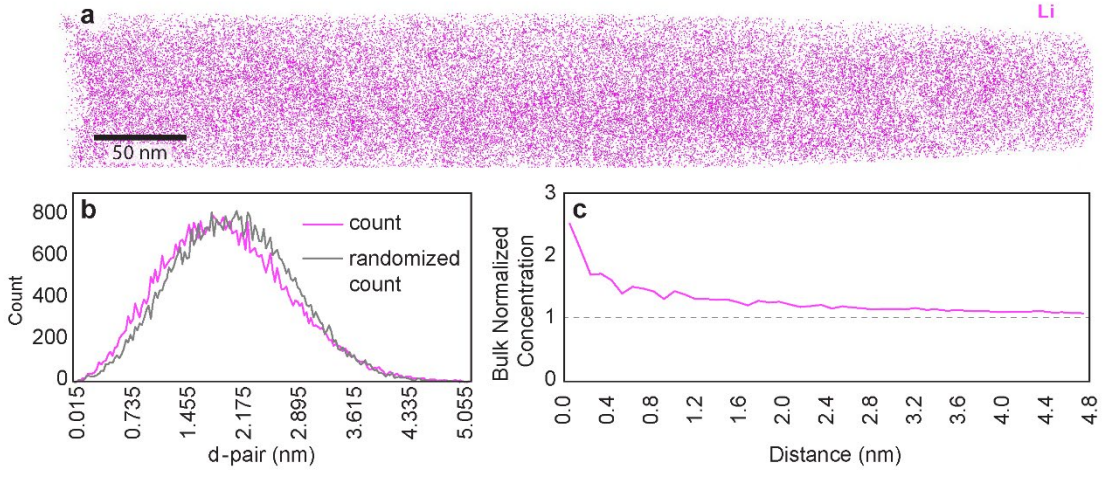

510

Figure 5. Li distribution analysis. Sample 05A-23.2. a: Li atom locations in tomographic reconstruction. b: Comparison of observed (pink) and expected (black) d-pair distance. c: Bulk normalized concentration of Li versus distance.

https://doi.org/10.5194/egusphere-2025-1810
Preprint. Discussion started: 16 May 2025

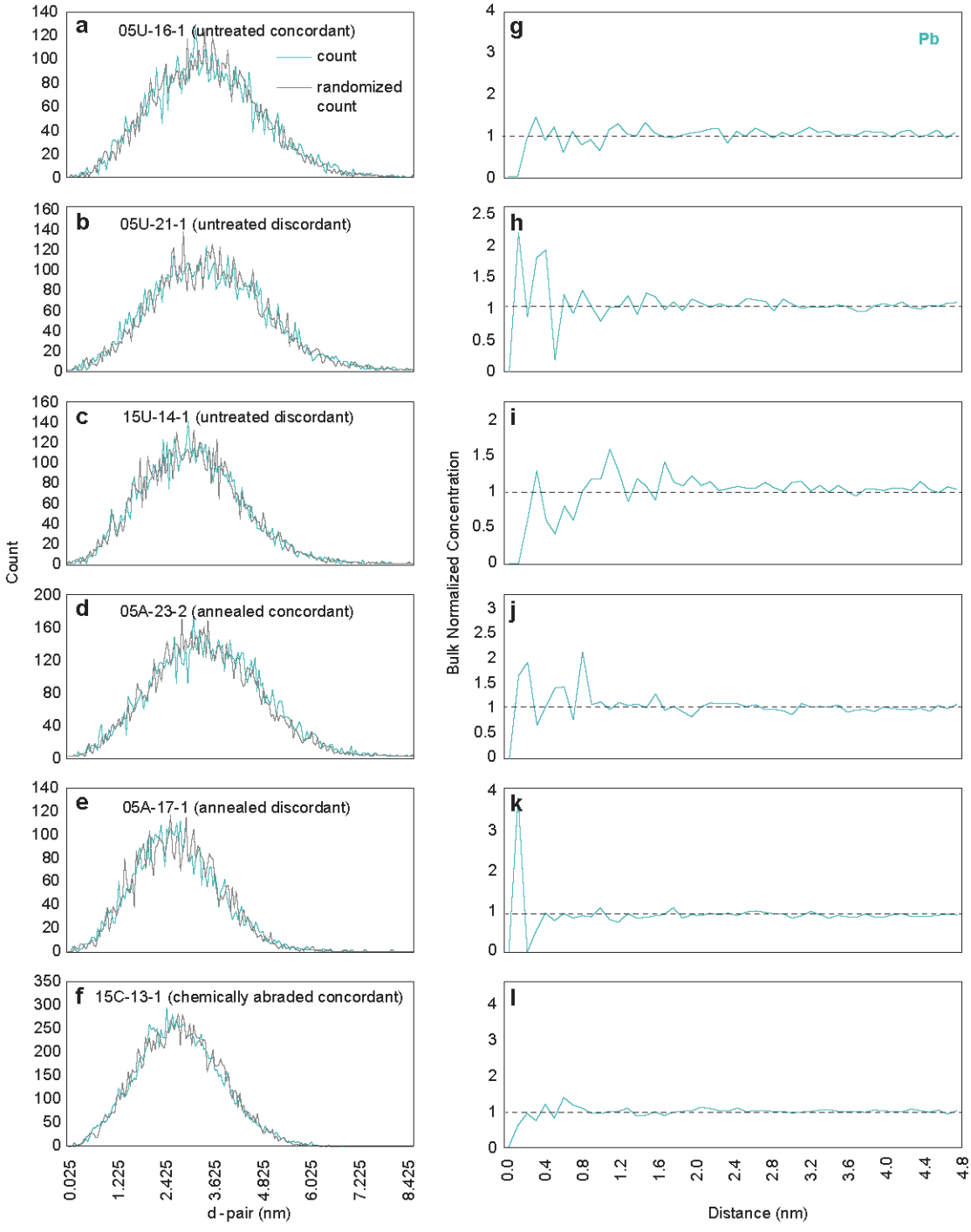

Figure 6. Pb distribution analysis. a-f count vs randomly generated count vs nearest neighbour distance. g-l: difference between random and measured counts vs distance.

https://doi.org/10.5194/egusphere-2025-1810
Preprint. Discussion started: 16 May 2025

Tables

Table 1. Population weighted mean geochronology results for OG1 analyses.

Mount	sample	$^{206}Pb/^{238}U$ ratio	Inter 2σ%	Exter 2σ%	$^{206}Pb/^{238}U$ Date	±X 2σ Ma	±Y 2σ Ma	MSWD	PoF	n (rej)	$^{207}Pb/^{206}Pb$ ratio	2σ er %	$^{207}Pb/^{206}Pb$ date	er, 2σ Ma	MSWD	PoF	n (rej)
GA5005	Untreated	0.705094	0.37	0.46	3439.9	9.9	12.5	0.74	0.82	40 (5)	0.29923	0.09	3466.2	1.5	0.85	0.73	40 (0)
GA5015	Untreated	0.704382	0.32	0.53	3437.2	8.7	11.6	0.88	0.74	41 (3)	0.29922	0.08	3466.2	1.3	0.73	0.90	41 (0)
GA5005	Annealed	0.711277	0.40	0.49	3463.3	10.8	13.2	0.55	0.94	40 (10)	0.29908	0.09	3465.4	1.5	0.98	0.50	40 (1)
GA5015	CA	0.712704	0.32	0.43	3468.6	8.8	11.6	0.55	0.96	40 (0)	0.29933	0.09	3466.8	1.4	1.23	0.16	40 (1)

MSWD= mean squared weighted deviation (χ^2/υ); PoF = probability of fit. Uncertainties are x/y as per Schoene et al. (2006)

Table 2. Geochronology results for spots subject to Raman mapping.

Mount	Spot	f 206 *	U (ppm)	Th (ppm)	$^{232}Th/^{238}U$	^{204}Pb-corr $^{238}U/^{206}Pb^*$	err (%)	^{204}Pb-corr $^{207}Ob^*/^{206}Pb^*$	err (%)	^{204}Pb-corr $^{206}Pb/^{238}U$ age (Ma)	1s err (Ma)	^{204}Pb-corr $^{207}Pb/^{206}Pb$ age (Ma)	1s err (Ma)	Disc.** (%)	Type
GA5015	15U-21.1	0.01	185	82	0.46	1.3968	1.0	0.29899	0.3	3481	26	3465	4	-0.6	Untreated concordant
GA5005	*05U-16.1*	*0.12*	*203*	*116*	*0.59*	*1.4169*	*1.3*	*0.29995*	*0.4*	*3443*	*35*	*3470*	*7*	*1.0*	*Untreated concordant*
GA5015	*15U-14.1*	*-0.01*	*201*	*98*	*0.50*	*1.4885*	*1.0*	*0.29944*	*0.3*	*3313*	*25*	*3467*	*4*	*5.7*	*Untreated discordant*
GA5005	*05U-21.1*	*0.00*	*380*	*274*	*0.74*	*1.4621*	*1.4*	*0.30017*	*0.4*	*3359*	*36*	*3471*	*6*	*4.1*	*Untreated discordant*
GA5005	A-23.1	0.29	265	340	1.32	1.4321	0.9	0.29983	0.2	3414	24	3469	4	2.1	Annealed concordant
GA5005	*A-23.2*	*-0.01*	*247*	*299*	*1.25*	*1.4034*	*0.9*	*0.30049*	*0.2*	*3468*	*25*	*3473*	*3*	*0.2*	*Annealed concordant*
GA5005	A-20.1	0.10	340	136	0.41	1.5661	1.6	0.29171	0.2	3183	41	3427	3	9.0	Annealed discordant
GA5005	*A-17.1*	*0.19*	*221*	*204*	*0.95*	*1.5166*	*1.1*	*0.30019*	*0.4*	*3265*	*27*	*3471*	*7*	*7.6*	*Annealed discordant*
GA5005	A-28.1	0.10	225	142	0.65	1.5086	1.7	0.29912	0.4	3278	43	3466	6	6.9	Annealed discordant
GA5015	*C-13.1*	*0.03*	*202*	*166*	*0.85*	*1.3996*	*1.0*	*0.29981*	*0.4*	*3475*	*26*	*3469*	*6*	*-0.2*	*CA concordant*
GA5015	C-17.1	0.00	197	158	0.83	1.4122	1.0	0.3	0.3	3451	26	3462	4	0.4	CA concordant

Note: Samples in italics were selected for APT analysis after Raman mapping.
* f 206 = common ^{206}Pb / total ^{206}Pb, calculated from the observed ^{204}Pb.
** U–Pb discordance; difference between the ^{204}Pb-corrected $^{206}Pb/^{238}U$ and $^{207}Pb/^{206}Pb$ ages.

Table 3. Raman results obtained in hyperspectral x-y maps.

Spot	Type	General description	$\nu_3(SiO_4)$ Raman band	
			Raman shift (cm^{-1})	FWHM (cm^{-1})
15U-21.1	Untreated concordant	Moderate radiation damage, no fine-scale zoning	999.3-1001.8	10.2-19
05U-16.1	*Untreated concordant*	*Moderate radiation damage, no fine-scale zoning*	*998.8-1000.1*	*12.5-22*
15U-14.1	*Untreated discordant*	*Moderate to severe radiation damage, no fine-scale zoning*	*997.0-1000.5*	*15-32*
05U-21.1	*Untreated discordant*	*Moderate to severe radiation damage, no fine-scale zoning*	*998.2-1000.4*	*15-30*

https://doi.org/10.5194/egusphere-2025-1810
Preprint. Discussion started: 16 May 2025

A-23.1	Annealed concordant	Mildly to moderately damaged, patchy zoning	1005.0-1007.2	4.5-9.2
A-23.2	*Annealed concordant*	*Mildly damaged, weak primary zoning*	*1006.7-1007.3*	*3.7-4.7*
A-20.1	Annealed discordant	Mildly to moderately damaged, fracture, patchy zoning	1004.0-1007.1	4.6-11.9
A-17.1	*Annealed discordant*	*Mildly damaged, weak primary zoning*	*1007.1-1007.7*	*3.2-5.4*
A-28.1	Annealed discordant	Mildly damaged, weak primary zoning	1005.1-1006.1	5.5-7.6
C-13.1	*CA (concordant)*	*Mildly damaged, weak primary zoning*	*1004.9-1005.9*	*5.5-7.7*
C-17.1	CA (concordant)	Mildly damaged, weak primary zoning	1005.4-1006.1	4.8-7.2

Note: Samples in italics were selected for APT analysis.

Table 4. Summary of APT results

Table 4. APT bulk composition analysis (at%)

	05U-16-1 (untreated concordant)			05U-21-1 (untreated discordant)			15U-14-1 (untreated discordant)			A-23-2 (annealed concordant)					A-17-1 (annealed discordant)			C-13-1 (chemically abraded)				
Dataset	**84840**	**84845**	**85062**	**82932**	**82937**	**83650**	**87032**	**87058**	**87473**	**78075**	**78174**	**78229**	**78402**	**78434**	**79815**	**79906**	**80175**	**85476**	**85586**	**85640**	**85690**	**85698**
H	5.785	6.529	7.210	3.467	5.261	5.010	1.712	2.287	1.138	2.309	3.389	2.118	5.845	6.762	5.922	9.323	8.555	5.245	8.827	10.83	4.459	3.386
O	58.81	57.86	58.07	60.22	59.81	60.54	61.14	62.27	61.71	60.54	59.66	60.28	57.47	57.45	58.75	57.28	57.56	58.37	56.86	55.56	59.62	60.20
Zr	19.90	19.99	19.53	20.30	19.25	19.21	20.59	19.25	20.52	20.71	20.77	21.06	20.62	19.81	19.70	18.54	18.66	20.09	18.85	17.43	18.68	19.90
Si	15.26	15.48	14.98	15.84	15.50	15.02	16.26	15.94	16.48	16.08	15.93	16.27	15.82	15.74	15.37	14.64	14.96	16.03	15.26	16.00	17.06	16.26
Y	0.046	0.039	0.043	0.032	0.026	0.028	0.033	0.026	0.020	0.111	0.080	0.087	0.077	0.081	0.071	0.068	0.070	0.034	0.025	0.025	0.036	0.052
Pb	0.017	0.001	0.002	0.003	0.007	0.000	0.008	0.004	0.005	0.006	0.005	0.003	0.003	0.009	0.009	0.007	0.001	0.004	0.006	0.003	0.005	0.007
Li	0.014	0.002	0.002	0.012	0.011	0.007	0.047	0.019	0.009	0.054	0.027	0.026	0.028	0.014	0.022	0.021	0.024	0.030	0.020	0.024	0.024	0.027
Th	0.000	0.001	0.000	0.000	0.000	0.004	0.000	0.001	0.000	0.000	0.003	0.000	0.004	0.000	0.007	0.002	0.000	0.004	-0.001	0.001	0.000	0.000
Yb	0.007	0.004	0.007	0.004	0.003	0.004	0.009	0.004	-0.006	0.008	0.005	0.006	0.003	0.004	0.006	0.002	0.006	0.008	0.004	0.001	0.002	0.006
Lu	0.000	0.001	0.001	0.001	0.000	0.004	0.001	0.004	0.003	0.002	0.001	0.002	0.002	0.001	0.001	-0.001	0.001	0.001	0.003	0.002	0.003	0.001
Hf	0.168	0.103	0.153	0.126	0.129	0.164	0.195	0.190	0.123	0.171	0.133	0.155	0.121	0.127	0.135	0.111	0.162	0.185	0.147	0.132	0.123	0.153
U	0.005	0.002	0.001	0.001	0.001	0.002	0.003	0.002	0.001	0.002	0.001	0.001	0.001	0.000	0.001	0.005	0.002	0.002	0.002	-0.001	-0.002	0.003
Tm	0.001	0.002	0.002	0.000	0.001	0.001	0.001	0.001	0.000	0.002	0.001	0.002	0.001	0.001	0.001	-0.002	0.001	0.000	0.002	-0.001	-0.002	0.002
Si2+/Si+	19.39	24.60	22.99	25.20	25.53	27.93	20.44	22.46	23.14	20.00	19.36	21.05	18.25	17.07	23.35	20.34	24.38	22.68	23.88	21.93	24.37	25.41

535